ACS APPLIED MATERIALS & INTERFACES

Research Article

Cite This: ACS Appl. Mater. Interfaces 2018, 10, 30548−30557

www.acsami.org

Manipulating Behaviors from Heavy Tungsten Doping on Interband Electronic Transition and Orbital Structure Variation of Vanadium Dioxide Films

Jiaoyan Zhou,[†] Mingzhang Xie,[†] Anyang Cui,[†] Bin Zhou,[†] Kai Jiang,[*,†] Liyan Shang,[†] Zhigao Hu,[*,†,‡] and Junhao Chu[†]

[†]Key Laboratory of Polar Materials and Devices (MOE) and Technical Center for Multifunctional Magneto-Optical Spectroscopy (Shanghai), Department of Electronic Engineering, East China Normal University, Shanghai 200241, China

[‡]Collaborative Innovation Center of Extreme Optics, Shanxi University, Taiyuan, Shanxi 030006, China

Downloaded via EAST CHINA NORMAL UNIV on March 25, 2019 at 06:35:47 (UTC).
See https://pubs.acs.org/sharingguidelines for options on how to legitimately share published articles.

ABSTRACT: Vanadium dioxide (VO_2) with a metal−insulator transition (MIT) has been supposed as a candidate for optoelectronic devices. However, the MIT temperature (T_{MIT}) above room temperature limits its application scope. Here, high-quality $V_{1-x}W_xO_2$ films have been prepared by pulsed laser deposition. On the basis of temperature-dependent transmittance and Raman spectra, it was found that T_{MIT} increases from 241 to 279 K, when increasing the doping concentration in the range of $0.16 \leq x \leq 0.20$. The interband electronic transitions and orbital structures of $V_{1-x}W_xO_2$ films have been investigated via fitting transmittance spectra. Moreover, with the aid of first-principles calculations, an effective orbital theory has been proposed to explain the unique phenomenon. When the W doping concentration increases, the π^* and d_{II} orbitals shift toward the π orbital. Meanwhile, the energy gap between the π^* and d_{II} orbitals decreases at the insulator state. It indicates that the bandwidth is narrowed, which impedes MIT. In addition, the overlap of the π^* and d_{II} orbitals increases at the metal state, and more doping electrons occupy the π^* orbital induced by increasing W doping concentration. It manifests that the Mott insulating state becomes more stable, which further improves T_{MIT}. The present work provides a feasible approach to tune T_{MIT} via orbital variation and can be helpful in developing the potential VO_2-based optoelectronic devices.

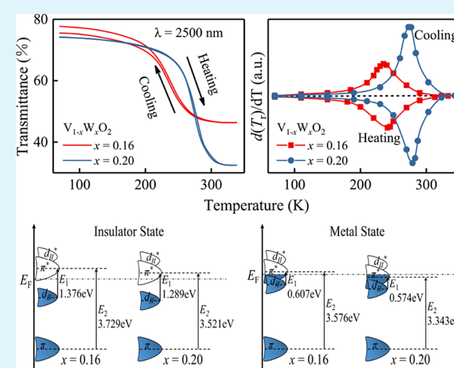

KEYWORDS: *vanadium dioxide, heavy tungsten doping, insulator−metal transition, first-principles calculations, orbital structure variation*

1. INTRODUCTION

Vanadium dioxide (VO_2) is a representative strongly correlated electronic material and has attracted a lot of interest, because of its excellent properties and prospective applications, as a tunable material in optical switches, field-effect transistors, and memristive elements.[1−4] It is well-known that VO_2 shows an invertible first-order metal−insulator transition (MIT) when the critical temperature (T_{MIT}) is ~340 K.[5,6] Meanwhile, the structure is distorted from the high-temperature rutile phase [VO_2(R), $P4_2/mnm$] to the low-temperature monoclinic phase [$VO_2(M_1)$, $P2_1/c$].[7−9] Furthermore, the structural distortion causes several orders of magnitude change in electrical resistivity and an abrupt decrease in infrared transmittance. The transition of pure VO_2 can be driven by Mott transition (electron−electron correlation), Peierls transition (electron-lattice dynamics), or collaborative Mott−Peierls transition, which is an intense debate.[10−12] Additionally, even if this material has been used in many advanced applications, the comparatively high MIT temperature (T_{MIT}) above room temperature limits its application scope.

Recently, great efforts have been made to manipulate VO_2 phase transition and lower its T_{MIT}, such as strain,[13] doping,[14−17] defect engineering,[18−20] and so on. Because of the nonuniformity of defect and strain engineering,[21] chemical doping[22−24] is a more effective means to dramatically alter T_{MIT}, such as tungsten (W),[25−27] neodymium (Nd),[28] molybdenum (Mo),[29,30] zirconium (Zr),[31] and magnesium (Mg)[32] doping. The W element is the most valid dopant, which can drop T_{MIT} below room temperature easily at a rate of 21−28 K/at. %.[33,34] As a typical example, Shibuya et al.[35] have fabricated the $V_{1-x}W_xO_2$ film by pulse laser deposition (PLD), which shows an unusual phase diagram: for $x \leq 0.07$, T_{MIT} decreases with increasing x, and a metallic stable state is discovered for $0.08 \leq x \leq 0.09$, whereas MIT reappears and T_{MIT} increases with increasing x for the case of $x \geq 0.1$. Nevertheless, the fundamental mechanism for heavy W doping modulating the MIT process has been still under debate.[36−38]

Received: June 13, 2018
Accepted: August 14, 2018
Published: August 14, 2018

ACS Publications © 2018 American Chemical Society

In the $V_{1-x}W_xO_2$ system, the W element acts as the donor, and the valence of W is only 6+, which amounts for increasing two V^{3+} ions and decreasing three V^{4+} ions per W^{6+} ion to keep charge neutrality.[39] From synchrotron radiation-based X-ray absorption spectroscopy (XAS) and first-principles calculations,[40] the results showed that the M-phase VO_2 is twisted to form R-phase VO_2 because of the symmetric W core. In addition, Sakai et al.[41] have used hard X-ray photoemission spectroscopy and XAS to illustrate the $V_{1-x}W_xO_2$ thin films, which suggested that the unusual phase diagram derives from the competition between the Peierls and Mott transitions. However, the influences of heavy W doping ($x \geq 0.1$) on the interband electronic transition and orbital structure have rarely been investigated to date. As a matter of fact, orbital configuration plays another vital role in investigating the physical properties of transition-metal oxides.[42] W^{6+} ions substituting V^{4+} ions inevitably induce additional electrons, which affect the orbital configuration further. Therefore, providing an additional view to study the VO_2 film heavily doped with W is necessary for understanding its mechanism and developing potential optoelectronic applications.

In this work, based on nondestructive optical measurements, we are the first to systematically study the $V_{1-x}W_xO_2$ films with a heavy doping concentration ($0.16 \leq x \leq 0.20$). Its influences on T_{MIT}, interband electronic transition, complex dielectric function, and orbital structure are discussed in detail. The variation of the MIT process and the increase of T_{MIT}, which is induced by heavy W doping, can be elucidated by the hysteresis behavior of the interband electronic transition. The unusual change of the interband electronic transition corresponds to the deviation of the orbital structure. With the aid of the first-principles calculations, the mechanism of the orbital variation induced by heavy W doping has been investigated in detail. In addition, the origin of manipulation on the phase transition of VO_2 through oxygen nonstoichiometry also has been discussed, which is different from the mechanism of the VO_2 film heavily doped with W. It suggests that the variation of orbital structure plays a critical role during the MIT process.

2. EXPERIMENTAL AND THEORETICAL SECTION

2.1. Fabrication of $V_{1-x}W_xO_2$ Films. The $V_{1-x}W_xO_2$ epitaxial films were grown on a single-crystal *c*-cut Al_2O_3 substrate by the PLD technique.[19] The substrates were cleaned in pure ethanol and acetone with an ultrasonic bath and flushed by deionized water several times. The VO_2/W (99/1 at. %) target was synthesized by VO_2 and W powders (purity 99.9%). The vacuum chamber was evacuated down to 6.75×10^{-4} mTorr. During the deposition process, deposition time, oxygen pressure, and energy density were varied to prepare the $V_{1-x}W_xO_2$ films with different W doping concentrations, which would be hereafter denoted S1−S12. The growth conditions are summarized in Table 1. Meanwhile, the substrate temperatures were kept at room temperature for all the films. After deposition, the amorphous films were annealed in an argon atmosphere at 450 °C for 1 h, which can make crystallization easier.

2.2. Characterization Methods. The thicknesses of the $V_{1-x}W_xO_2$ films were obtained by a scanning electron microscope (Philips XL30FEG), which is equipped with an energy-dispersive X-ray spectrometer. As shown in Table 1, the thickness increases from 19.2 to 32.0 nm. The structural characteristics were analyzed by X-ray diffraction (XRD, Bruker D8 Advance diffractometer) with Cu Kα radiation (λ = 1.5418 Å) at room temperature. Atomic force microscopy (AFM, Digital Instruments Icon, Bruker) was used to investigate the surface morphology. X-ray photoelectron spectroscopy (XPS, RBD-upgraded PHI-5000C ESCA system, PerkinElmer) with Mg Kα radiation ($h\nu$ = 1253.6 eV) was carried out to analyze the stoichiometries and valences state of the films. A double-beam ultraviolet−infrared spectrophotometer (PerkinElmer Lambda 950) was employed to record the normal−incident transmittance spectra in the photon energy range from 0.5 to 6.5 eV (2650−190 nm) with a spectral resolution of 2 nm. An optical cryostat (Janis SHI-4-1) and a heating stage (Bruker A599) were used for low-temperature and high-temperature experiments, respectively. The temperature can be varied from 70 to 343 K. Temperature-dependent Raman spectra were detected by a Jobin-Yvon LabRAM HR Evolution spectrometer and a THMSE 600 heating/cooling stage (Linkam Scientific Instruments) in the range of 80−300 K. To characterize the temperature-dependent electrical properties, the resistances were measured by a Keithley model 6430 Sub-Femtoamp Remote SourceMeter and a THMSE 600 heating/cooling stage (Linkam Scientific Instruments) from 90 to 373 K.

Table 1. Different Growth Conditions and Thicknesses of S1−S12 Films

samp.	energy density (J cm^{-2})	oxygen pressure (mTorr)	deposition time (min)	thickness (nm)
S1	2.47	5	67	20.3
S2	2.47	5	100	24.0
S3	2.65	5	67	21.9
S4	2.65	5	100	25.7
S5	2.65	10	33	19.2
S6	2.65	10	67	23.7
S7	2.65	10	100	27.0
S8	2.83	5	67	25.4
S9	2.83	5	100	29.9
S10	2.83	10	33	22.0
S11	2.83	10	67	27.5
S12	2.83	10	100	32.0

2.3. Theoretical Calculations. The band structures and density of states (DOS) of the pure VO_2(M) and $V_{1-x}W_xO_2$(M) systems were calculated by first-principles theory calculations. The density functional theory calculations were carried out with the plane-wave pseudopotentials and generalized gradient approximation (GGA) in the form of Perdew−Burke−Ernzerhof exchange−correlation functional. Because of the presence of V 3d electrons, the Hubbard-type correction U was used to explain the intense on-site Coulomb repulsion. Meanwhile, the effective value of $U_{eff} = U - J$ was selected to be 3.4 eV, which was consistent with the optimal values of U and Hund's exchange interaction J reported by Biermann et al.[8] Recently, the GGA + U method (U_{eff} = 3.4 eV) has been widely used to accurately investigate the energy band and electronic structure of VO_2.[8,43] The supercells with 2 × 2 × 2 primitive unit cells for the monoclinic phase were constructed in our calculations. The cutoff energy for the plane-wave basis set is 550 eV, and Brillouin zones are sampled using 3 × 3 × 3 Monkhorst−Pack k points for geometry optimization and self-consistent calculation to ensure good convergence of the computed structures and energies, respectively. The structures were fully optimized until the Hellmann−Feynman forces were less than 0.01 eV/Å. The convergence criterion of energy tolerance was 1.0×10^{-5} eV/atom in geometry optimization and self-consistent field calculation. To calculate the electronic DOS, we used a 5 × 5 × 5 k-point mesh and the linear tetrahedron method with Blöchl corrections for VO_2(M). Here, the V atom is replaced by W atom in the dopant cases. To acquire reasonable results, we calculated several different dopant positions and obtained the most stable doped structure for property calculations. According to the previous report by Sun et al.,[44] the free energies of VO_2(M) along with enthalpies and stabilities have not been dramatically affected when nonspin polarization is performed in the GGA + U method. Hence, our calculations were executed without spin polarization, in accordance with the previous reports.[43,44]

DOI: 10.1021/acsami.8b09909
ACS Appl. Mater. Interfaces 2018, 10, 30548−30557

3. RESULTS AND DISCUSSION

3.1. Structural Analysis. The XRD patterns of the $V_{1-x}W_xO_2$ films were measured at room temperature. The typical samples were selected to verify the film structure, as shown in Figure 1a. The diffraction peaks were located at 2θ = 27.7°, which corresponds to the (110) plane from the rutile phase of VO_2 (JCPDS no. 44-0253). It suggests that T_{MIT} is under room temperature. Moreover, the XRD results indicate that the films can be grown along the preferred (110) plane, which is consistent with the results measured with the Raman spectra at 300 K. It indicates that the $V_{1-x}W_xO_2$ films have a pure phase at room temperature, with good uniformity. The extra diffraction peak near 27.7° is supposed to be derived from the substrate.

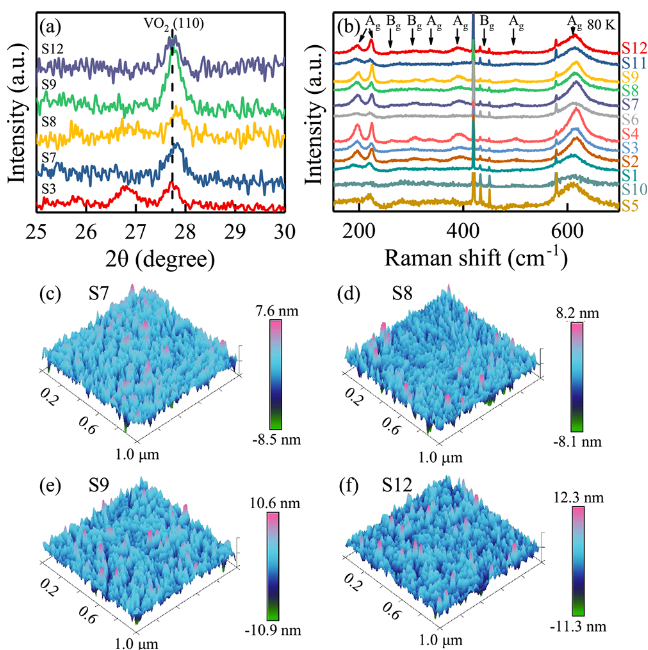

Figure 1. (a) XRD patterns of the $V_{1-x}W_xO_2$ films under different growth conditions. (b) Raman spectra of all the films measured at 80 K. AFM images of (c) S7, (d) S8, (e) S9, and (f) S12 films.

Figure 1b shows the Raman spectra of the $V_{1-x}W_xO_2$ films measured at 80 K, and the phonon modes can be assigned. The obvious peaks at 196, 223, and 614 cm^{-1} reveal that the $V_{1-x}W_xO_2$ films with high-quality crystallization are of the pure monoclinic phase at 80 K. The A_g phonon modes are located at around 196, 223, 337, 387, 498, and 614 cm^{-1}. The weaker peaks at around 260, 303, and 442 cm^{-1} correspond to the B_g phonon modes. The phonon frequencies are in agreement with the previous reports.[45−50] The A_g phonon mode at 614 cm^{-1} is the characteristic of V−O vibration. The two A_g phonon modes at 196 and 223 cm^{-1} are related to the shift of V ions along the dimerized chains. The shift of the peaks between different samples is due to the vibration of V−O and the dimerization of V ions. The additional peaks in Raman spectra are derived from the *c*-cut Al_2O_3 substrate. As shown in Figure 1c−f, the three-dimensional AFM images show the surface morphologies, and the root-mean-square surface roughnesses of S7, S8, S9, and S12 are 1.65, 1.41, 2.05, and 2.07 nm, respectively. It indicates that the increasing thickness cannot obviously affect the surface roughness, although the variation of deposition time, oxygen pressure, and energy density can change the thickness.

3.2. XPS Analysis. From Table 1, 12 $V_{1-x}W_xO_2$ films can be divided into three groups based on different growth parameters (deposition time, oxygen pressure, and energy density). To study the influence of the three growth parameters on W-doping concentration, the XPS spectra of typical samples including S2−S4, S7, and S9 were measured. Figure 2a shows the overall core-level XPS spectra.

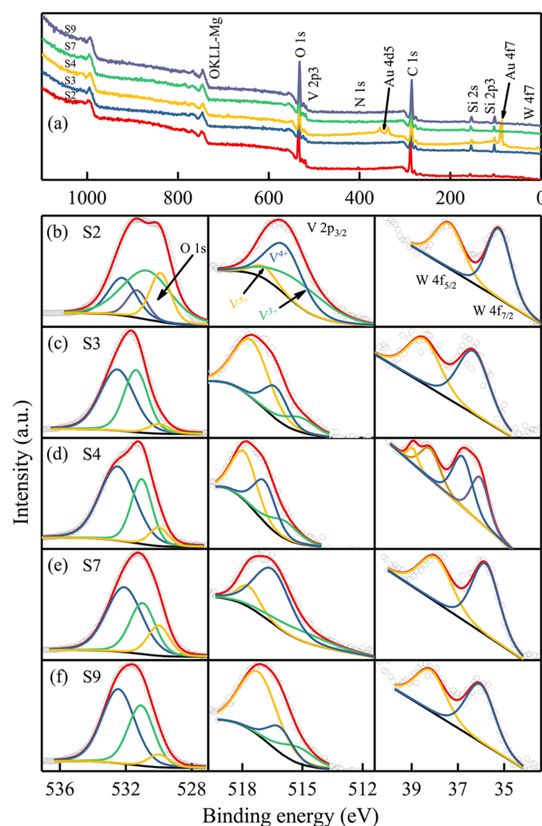

Figure 2. (a) Overall XPS spectra of the $V_{1-x}W_xO_2$ films. High-resolution XPS spectra of O 1s, V $2p_{3/2}$, and W 4f of (b) S2, (c) S3, (d) S4, (e) S7, and (f) S9 films, respectively.

For analyzing the stoichiometries and valence states of the $V_{1-x}W_xO_2$ films, high-resolution XPS spectra are implemented in the binding energy regions of O 1s, V $2p_{3/2}$, and W 4f, as shown in Figure 2b−f. The binding energy of C 1s is marked at 284.8 eV as the reference. Under different growth conditions, the W 4f scans can be precisely split into W $4f_{5/2}$ and W $4f_{7/2}$ peaks, which are located in the range of 39.0−37.4 eV and 36.8−35.2 eV, respectively. They are both assigned to W^{6+}, which indicates that W has been totally oxidized and successfully incorporated into the VO_2 lattice. For V $2p_{3/2}$ scans, the peaks are split into V^{4+} (around 516 eV), V^{3+} (around 515 eV), and V^{5+} (around 517 eV) peaks, respectively.[51,52] The presence of V^{3+} peaks is due to the incorporation of W^{6+} and the substitution of V^{4+}. For W doping, the V^{4+}−V^{4+} bonds are broken down to form V^{3+}−W^{6+} and V^{3+}−V^{4+} pairs for charge compensation.[39] In addition, the appearance of V^{5+} peaks is connected with surface oxygenic composition. For O 1s scans, the peak located at around 530.0 eV can be assigned to O 1s. The additional peaks located at around 531 and 532.3 eV can be assigned to C═O and C−

DOI: 10.1021/acsami.8b09909
ACS Appl. Mater. Interfaces 2018, 10, 30548−30557

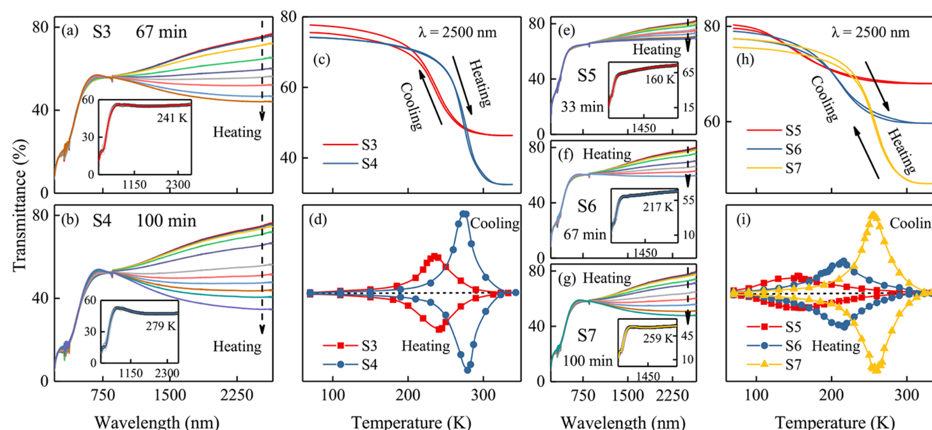

Figure 3. Transmittance spectra of the $V_{1-x}W_xO_2$ films prepared at different deposition times: (a) S3, (b) S4, (e) S5, (f) S6, (g) S7 films, respectively. The best-fitted (solid line) and experimental (dotted line) transmittance spectra are shown in the inset. (c) Temperature-dependent infrared transmittance at the selected wavelength (λ = 2500 nm) and (d) differential curves of $(S3{\cdot}S4)_{G1}$. (h) Hysteresis loops of infrared transmittance (at λ = 2500 nm) and (i) differential curves of $(S5{\cdot}S6{\cdot}S7)_{G1}$.

O(H), respectively, on account of the surface adsorption of oxygen and oxidized carbons originating from the preparation process.[51] The XPS results show that the V^{5+} peaks are broadening with expanding C═O and C−O(H) peaks because the film surfaces are overoxidized. Furthermore, the relative doping concentration of tungsten $[c_W/(c_W + c_V)]$ and oxygen stoichiometry $[c_O/(c_V + c_W)]$ have been calculated from the XPS spectra. The stoichiometries of S2−S4, S7, and S9 are $V_{0.811}W_{0.187}O_{1.990}$, $V_{0.84}W_{0.160}O_{2.002}$, $V_{0.8}W_{0.200}O_{2.006}$, $V_{0.822}W_{0.178}O_{2.090}$, and $V_{0.805}W_{0.195}O_{2.004}$, respectively. Because of the thin thickness of the $V_{1-x}W_xO_2$ film, XPS analysis can accurately reflect the general information of the whole film. Moreover, the results of the relative doping concentration of tungsten are similar with those from energy-dispersive X-ray spectrometry, which further demonstrate the good uniformity of the $V_{1-x}W_xO_2$ film. It is found that all $V_{1-x}W_xO_2$ films are heavily doped by W ions ($x \geq 0.1$) and the W concentration increases with increasing deposition time and decreasing oxygen pressure. In addition, the $V_{0.8}W_{0.200}O_{2.006}$ [S4] film grown at an energy density of 2.65 J cm^{-2} contains the highest W concentration, compared with the other films $V_{0.811}W_{0.187}O_{1.990}$ [S2] and $V_{0.805}W_{0.195}O_{2.004}$ [S9] grown at the energy densities of 2.47 and 2.83 J cm^{-2}, respectively. As shown in Figure 2b−f, the W $4f_{7/2}$ peak shifts to a higher binding energy with increasing tungsten concentration.

3.3. Transmittance and Raman Spectra. As mentioned above, 12 $V_{1-x}W_xO_2$ films are divided into three matched groups. To investigate the effect of deposition time, $(S1{\cdot}S2)_{G1}$, $(S3{\cdot}S4)_{G1}$, $(S5{\cdot}S6{\cdot}S7)_{G1}$, $(S8{\cdot}S9)_{G1}$, and $(S10{\cdot}S11{\cdot}S12)_{G1}$ are assigned to group 1. $(S3{\cdot}S6)_{G2}$, $(S4{\cdot}S7)_{G2}$, $(S8{\cdot}S11)_{G2}$, and $(S9{\cdot}S12)_{G2}$ are assigned to group 2 to explain the influence of oxygen pressure during the process of deposition. Moreover, group 3 including $(S1{\cdot}S3{\cdot}S8)_{G3}$, $(S2{\cdot}S4{\cdot}S9)_{G3}$, $(S5{\cdot}S10)_{G3}$, $(S6{\cdot}S11)_{G3}$, and $(S7{\cdot}S12)_{G3}$ is used to investigate the influence of energy density.

To investigate the effect of deposition time, the temperature-dependent transmittance spectral experiments of S3−S7 films have been carried out from 70 to 300 K, as shown in Figure 3a,b,e−g. Figure 3c,h shows the hysteresis loops of infrared transmittance at a selected incident photon energy ($h\nu$ = 0.496 eV, λ = 2500 nm). The transmittance variations (ΔT_r) of $(S3{\cdot}S4)_{G1}$ and $(S5{\cdot}S6{\cdot}S7)_{G1}$ during the heating process are $(31.3\%, 41.7\%)_{G1}$ and (11.6%, 19.3%, 30.4%), respectively. The differential curves of transmittance versus temperature are shown in Figure 3d,i. The T_{MIT} values of $(S3{\cdot}S4)_{G1}$ and $(S5{\cdot}S6{\cdot}S7)_{G1}$ during the heating process are $(241\ K, 279\ K)_{G1}$ and $(160\ K, 217\ K, 259\ K)_{G1}$, respectively. Meanwhile, the full width at half-maximum (fwhm) decreases with increasing deposition time. In contrast to the variation of fwhm, ΔT_r and T_{MIT} increase significantly with increasing deposition time. Note that $(S3{\cdot}S4)_{G1}$ and $(S5{\cdot}S6{\cdot}S7)_{G1}$ show the same variation trend, as shown in Figure 3, which indicates that the effects from $(S3{\cdot}S4)_{G1}$ are similar to that from $(S5{\cdot}S6{\cdot}S7)_{G1}$. Comparing the stoichiometry of S3 ($V_{0.84}W_{0.160}O_{2.002}$) with that of S4 ($V_{0.8}W_{0.200}O_{2.006}$), the films show similar oxygen stoichiometry, whereas the W doping concentration of S4 is higher than S3, which indicates that the doping level increases with increasing deposition time. This demonstrates that the significant increase of T_{MIT} from 241 to 279 K is merely because of the heavy W doping concentration (x increases from 0.16 to 0.20), in accordance with the previous reports by Shibuya et al.[35] Moreover, increasing W doping concentration also enlarges the ΔT_r value from 31.3 to 41.7%. The results from the cooling process are the same as those from the heating process. Moreover, the width of the hysteresis loop of transmittance at the selected incident wavelength (λ = 2500 nm) is tiny. The largest discrepancy of T_{MIT} is less than 6 K, which is different from the pure VO_2 film.

To understand the influence of oxygen pressure during the deposition process, the transmittance spectra of $(S4{\cdot}S7)_{G2}$ from 70 to 300 K have been measured, as shown in Figure 4a,b. Figure 4c,d shows ΔT_r at the selected incident wavelength (λ = 2500 nm) and T_{MIT} during the heating process of $(S4{\cdot}S7)_{G2}$, which are $(41.7\%, 30.4\%)_{G2}$ and $(279\ K, 259\ K)_{G2}$, respectively. Comparing the stoichiometry of S4 ($V_{0.8}W_{0.200}O_{2.006}$) with that of S7 ($V_{0.822}W_{0.178}O_{2.090}$), the decreasing ΔT_r and T_{MIT} can be attributed to the reduction of W doping concentration (from 0.200 to 0.178). It means that increasing oxygen pressure can decrease the doping level. However, the variation rate of T_{MIT} of $(S4{\cdot}S7)_{G2}$ is less than that of $(S3{\cdot}S4)_{G1}$. This can be attributed to the fact that there is a larger oxygen stoichiometry for the $V_{0.822}W_{0.178}O_{2.090}$ [S7] film than for the $V_{0.8}W_{0.200}O_{2.006}$ [S4] film, with the $c_O/(c_V + c_W)$ ratio exceeding 2. Zhang et al.[19] have reported that the MIT characteristic of the VO_2 film is sensitive to oxygen stoichiometry and that the exceeding oxygen can slightly

DOI: 10.1021/acsami.8b09909
ACS Appl. Mater. Interfaces 2018, 10, 30548−30557

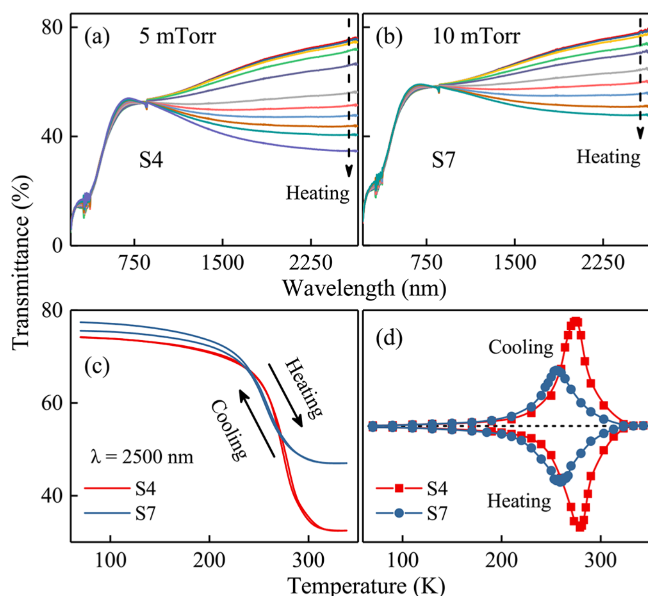

Figure 4. Transmittance spectra of the $V_{1-x}W_xO_2$ films prepared at different oxygen pressures: (a) S4 ($V_{0.8}W_{0.200}O_{2.006}$) and (b) S7 ($V_{0.822}W_{0.178}O_{2.090}$) films. (c) Temperature-dependent infrared transmittance (λ = 2500 nm) and (d) differential curves of $(S4{\cdot}S7)_{G2}$.

improve T_{MIT}. For investigating the effect of energy density, the transmittance experiments of $(S2{\cdot}S4{\cdot}S9)_{G3}$ have been recorded during the heating process at 70−300 K, as shown in Figure 5a−c. Figure 5d,e shows the temperature-dependent transmittance (at λ = 2500 nm) and resistivity, with the homologous differential curves in the inset. During the heating process, ΔT_r at the definite wavelength (λ = 2500 nm) of $(S2{\cdot}S4{\cdot}S9)_{G3}$ is $(37.0\%, 41.7\%, 39.1\%)_{G3}$. The resistivity of the

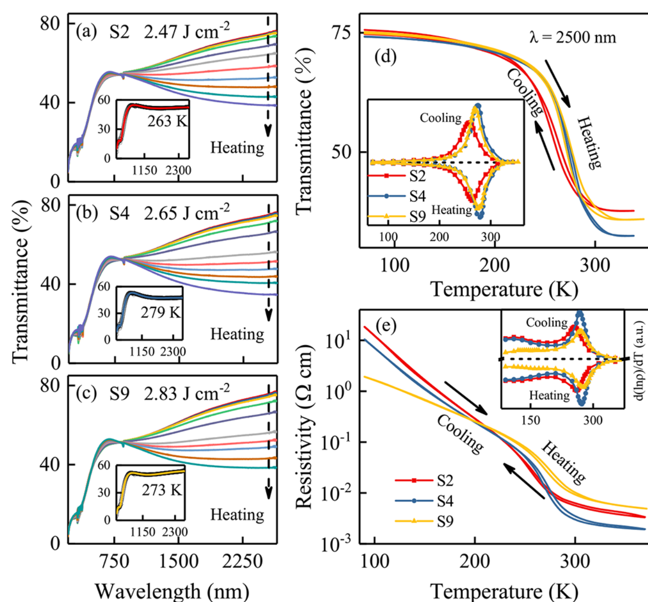

Figure 5. Transmittance spectra of the $V_{1-x}W_xO_2$ films prepared at different energy densities: (a) S2 ($V_{0.811}W_{0.187}O_{1.990}$), (b) S4 ($V_{0.8}W_{0.200}O_{2.006}$), and (c) S9 ($V_{0.805}W_{0.195}O_{2.004}$) films. The best-fitted (solid line) and experimental (dotted line) transmittance spectra are shown in the inset. (d) Temperature-dependent infrared transmittance (λ = 2500 nm) and (e) hysteresis loops of resistivity for $(S2{\cdot}S4{\cdot}S9)_{G3}$. The differential curves are shown in the inset.

$V_{0.811}W_{0.187}O_{1.990}$ [S2] and $V_{0.805}W_{0.195}O_{2.004}$ [S9] films sustains a low value of less than 10^{-2} Ω cm after MIT, whereas the $V_{0.8}W_{0.200}O_{2.006}$ [S4] film maintains the minimum value of resistivity. Notably, the decrease of resistivity is related to the electron concentration at the metal state. In addition, the variation in the resistivity of the $V_{0.8}W_{0.200}O_{2.006}$ [S4] film exceeds 3 orders of magnitude, which suggests that the S4 ($V_{0.8}W_{0.200}O_{2.006}$) film exhibits the good MIT characteristic, from which maximal ΔT_r and resistivity variation can be discovered. The T_{MIT} value of $(S2{\cdot}S4{\cdot}S9)_{G3}$ is $(263\text{ K}, 279\text{ K}, 273\text{ K})_{G3}$. Moreover, the $V_{0.8}W_{0.200}O_{2.006}$ [S4] film, which is synthesized at an energy density of 2.65 J cm^{-2}, contains the highest tungsten concentration than the $V_{0.811}W_{0.187}O_{1.990}$ [S2] and $V_{0.805}W_{0.195}O_{2.004}$ [S9] films. This indicates that T_{MIT} increases with increasing W doping concentration, which is consistent with the results from group 1 and group 2. Nevertheless, there is less oxygen stoichiometry for the $V_{0.811}W_{0.187}O_{1.990}$ [S2] film. Goodenough et al.[54] have reported that T_{MIT} cannot be depressed of nonstoichiometric $VO_{2+\epsilon}$ owing to the lack of π^* electrons. This indicates that T_{MIT} can be depressed by oxygen vacancies, which produce electrons to occupy the π^* orbital.

Figure 6 shows the temperature-dependent Raman spectra of S2−S5, S7, and S9, which correspond to the variation in the

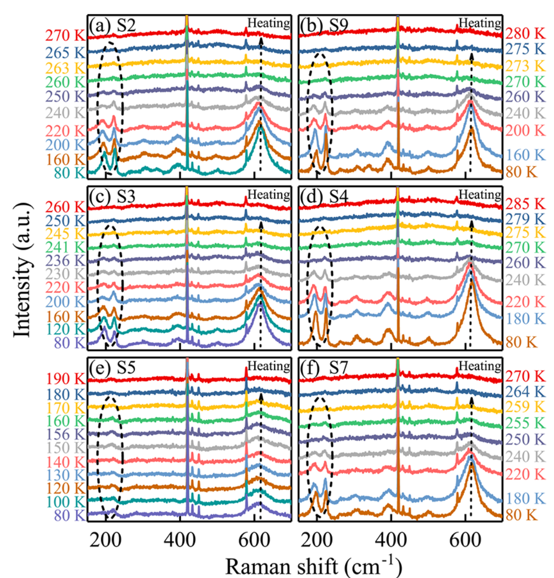

Figure 6. Raman spectra of (a) S2, (b) S9, (c) S3, (d) S4, (e) S5, and (f) S7 films during the heating process.

lattice. During the heating process, the phonon modes of the monoclinic phase gradually soften and disappear ultimately around T_{MIT}, owing to the generation of the rutile phase. The variation of the Raman peaks around T_{MIT} is in accordance with the temperature-dependent transmittance (at λ = 2500 nm) and resistivity. Moreover, according to the comparison of the Raman spectra at 80 K between S3 ($V_{0.84}W_{0.160}O_{2.002}$) and S4 ($V_{0.8}W_{0.200}O_{2.006}$), the small blue shifts of the obvious A_g modes 194.8, 223.4, and 614.4 cm^{-1} to 196.5, 224.4, and 616.2 cm^{-1} are confirmed, which is consistent with the results caused by light W doping.[53] It indicates that the crystal structure variation is not responsible for the unusual phase diagram in the heavy W doping range. However, based on the variation of fwhm, the enlargement of ΔT_r with increasing W doping concentration is supposed to be attributed to the crystal quality

DOI: 10.1021/acsami.8b09909
ACS Appl. Mater. Interfaces 2018, 10, 30548−30557

of the $V_{1-x}W_xO_2$ films. Figure 7 summarizes the relationship between ΔT_r (at λ = 2500 nm) and T_{MIT} with different growth

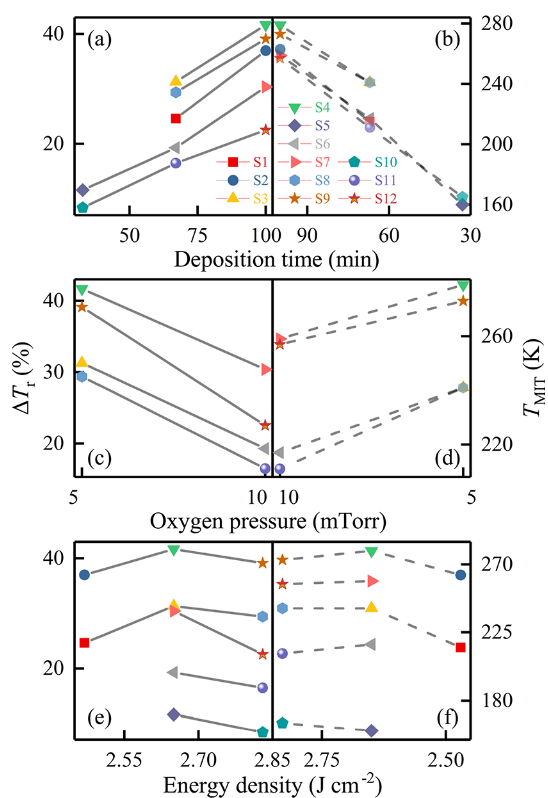

Figure 7. Relationship between the variations of infrared transmittance (ΔT_r) measured at 2500 nm and MIT temperature (T_{MIT}) with different growth parameters including (a,b) deposition time—group 1, (c,d) oxygen pressure—group 2, and (e,f) energy density—group 3.

parameters, including the deposition time, oxygen pressure, and energy density. Note that it shows the same variation tendency for the individual matched groups. The ΔT_r (at λ = 2500 nm) and T_{MIT} values increase significantly with increasing deposition time and decreasing oxygen pressure. Besides, the film synthesized at an energy density of 2.65 J cm^{-2} shows the largest ΔT_r and the maximum T_{MIT}, as compared with the films synthesized at the energy densities of 2.47 and 2.83 J cm^{-2}. On the basis of the three matched groups $(S3{\cdot}S4)_{G1}$, $(S4{\cdot}S7)_{G2}$, and $(S2{\cdot}S4{\cdot}S9)_{G3}$, along with the stoichiometries of S2 ($V_{0.811}W_{0.187}O_{1.990}$), S3 ($V_{0.84}W_{0.160}O_{2.002}$), S4 ($V_{0.8}W_{0.200}O_{2.006}$), S7 ($V_{0.822}W_{0.178}O_{2.090}$), and S9 ($V_{0.805}W_{0.195}O_{2.004}$), it is suggested that the T_{MIT} and ΔT_r (at λ = 2500 nm) values are obviously improved when the W doping concentration increases. Moreover, the oxygen vacancies inversely depress T_{MIT}, whereas the exceeding oxygen slightly rises T_{MIT}. This phenomenon may be related to the doping concentration of electrons generated by W doping and the variation of the orbital structure.

3.4. Complex Dielectric Function. To investigate the influence of heavy W doping on the complex dielectric function and interband electronic transition, a three-layered structure (air−film−substrate) with a Drude−Lorentz oscillator dispersion model has been considered to fit the transmittance spectra as follows

$$\varepsilon(E) = \varepsilon_1 + i\varepsilon_2 = \varepsilon_\infty - \frac{A_d}{E^2 + iEB_d} + \sum_{i=1}^{3} \frac{A_i}{E_i^2 - E^2 - iEB_i} \quad (1)$$

where ε_1 and ε_2 are the real and imaginary parts of the complex dielectric function, respectively; ε_∞ is the high-frequency dielectric constant; A_i, B_i, E_i, and E are the amplitude, broadening of the i-th oscillator, center energy, and incident photon energy, respectively; A_d and B_d are the squares of plasma frequency and damping frequency, respectively. This method has been proven to accurately investigate the mechanism of the pure VO_2 film.[19] During the fitting process, the parameters of A_i, B_i, E_i, A_d, and B_d are optimized to approach the experimental values. The best-fitted transmittance spectra can be observed in the insets of Figures 3a,b,e−g and 5a−c, indicating the reliable oscillator dispersion model.

The illustrations of Figure 8 present the best-fitted transmittance spectra versus photon energy. The imaginary

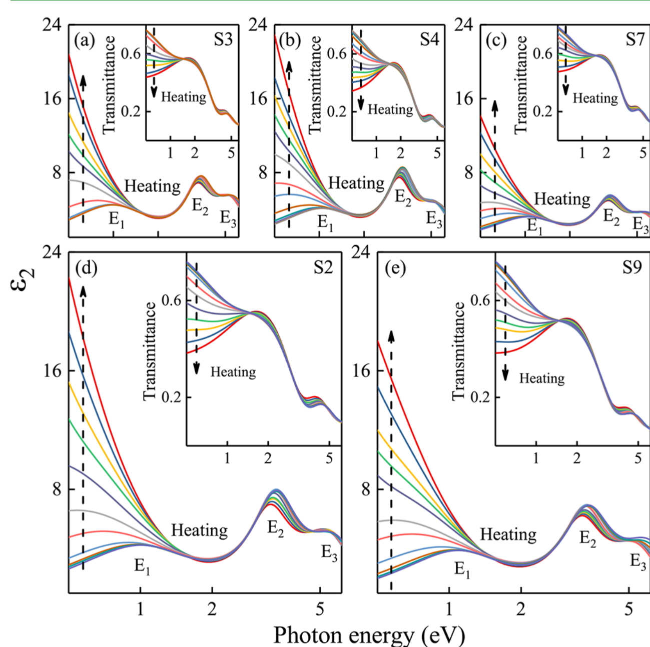

Figure 8. Imaginary parts of the complex dielectric functions ε_2 of (a) S3 ($V_{0.84}W_{0.160}O_{2.002}$), (b) S4 ($V_{0.8}W_{0.200}O_{2.006}$), (c) S7 ($V_{0.822}W_{0.178}O_{2.090}$), (d) S2 ($V_{0.811}W_{0.187}O_{1.990}$), and (e) S9 ($V_{0.805}W_{0.195}O_{2.004}$) films. The insets show the best-fitted transmittance spectra vs photon energy.

parts ε_2 of the complex dielectric functions of S2−S4, S7, and S9 with different tungsten and oxygen stoichiometries are shown in Figure 8. During the heating process, it is obviously observed that ε_2 dramatically improves with increasing the temperature at the region of near-infrared, particularly around T_{MIT}, which implies the formation of a metal state. Moreover, when the photon energy is below around 1.3 eV, the variation of ε_2 ($\Delta\varepsilon_2$) is 19.6, 17.9, 20.5, 12.3, and 16.0 for S2 ($V_{0.811}W_{0.187}O_{1.990}$), S3 ($V_{0.84}W_{0.160}O_{2.002}$), S4 ($V_{0.8}W_{0.200}O_{2.006}$), S7 ($V_{0.822}W_{0.178}O_{2.090}$), and S9 ($V_{0.805}W_{0.195}O_{2.004}$), respectively. As for $(S3{\cdot}S4)_{G1}$, $(S4{\cdot}S7)_{G2}$, and $(S2{\cdot}S4{\cdot}S9)_{G3}$, $\Delta\varepsilon_2$ increases with increasing W doping concentration. The variation of $\Delta\varepsilon_2$ is related to the electrical properties, which can be attributed to the fact that increasing

DOI: 10.1021/acsami.8b09909
ACS Appl. Mater. Interfaces 2018, 10, 30548−30557

W doping concentration introduces more extra electrons and improves carrier concentration.

3.5. Electronic Transition and Orbital Structure. The variation of ε_2 confirms three different interband electronic transitions, as shown in Figure 8, which can be assigned as follows: (1) E_1 is assigned to the transition from the lower V 3d filled d_{II} orbital to the empty π^* orbital, (2) E_2 is due to the transition from the O 2p filled π orbital to the empty π^* orbital, (3) E_3 corresponds to the transition from the lower V 3d filled d_{II} orbital to the empty σ^* orbital. The temperature-dependent interband electronic transitions E_1 and E_2 of the three typical matched groups $(S3{\cdot}S4)_{G1}$, $(S4{\cdot}S7)_{G2}$, and $(S2{\cdot}S4{\cdot}S9)_{G3}$ are shown in Figure 9. The hysteresis loops of E_1 and E_2 are similar to that of the temperature-dependent infrared transmittance at the selected incident wavelength (λ = 2500 nm). The interband electronic transition is intimately related to the orbital variation. As reported by Goodenough et al.,[54] a band gap is the difference between the bottom of the conduction band (E_c) and the top of the valence band (E_v). Moreover, E_c and E_v are the bottom of the π^* orbital and the top of the d_{II} orbital.

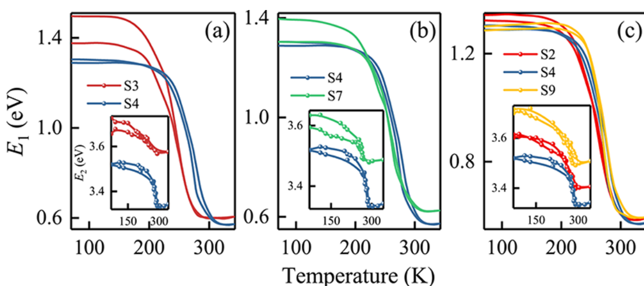

Figure 9. Temperature-dependent interband electronic transition E_1 of (a) $(S3{\cdot}S4)_{G1}$, (b) $(S4{\cdot}S7)_{G2}$, and (c) $(S2{\cdot}S4{\cdot}S9)_{G3}$. The insets show the hysteresis loops of E_2.

To investigate the influence of heavy W doping and oxygen nonstoichiometry on the variation of the orbital structure, the films S2−S4 and S7 along with S9 have been comprehensively considered. At 70 K, the films are at the insulator monoclinic structure. Meanwhile, the values of E_1 are 1.376, 1.286, and 1.289 eV for S3 ($V_{0.84}W_{0.160}O_{2.002}$), S9 ($V_{0.805}W_{0.195}O_{2.004}$), and S4 ($V_{0.8}W_{0.200}O_{2.006}$), respectively. Similarly, the values of E_2 are 3.729, 3.715, and 3.521 eV for S3, S9, and S4, respectively. This suggests that the increase of W doping concentration changes the orbital structure and decreases the interband electronic transitions. As shown in Figure 10a, when the W doping concentration increases, both the empty π^* orbital and the lower V 3d filled d_{II} orbital slightly shift to the O 2p filled π orbital, with the corresponding decrease of E_2 and $\Delta(E_2 - E_1)$. The reduction of E_1 means that the energy gap between the empty π^* orbital and the lower V 3d filled d_{II} orbital is decreased. However, there is larger E_2 and smaller E_1 for the $V_{0.805}W_{0.195}O_{2.004}$ [S9] film, compared to the $V_{0.8}W_{0.200}O_{2.006}$ [S4] film. It corresponds to the fact that the filled π orbital keeps away from E_F, whereas the filled d_{II} orbital becomes close to it. It might be induced by the thickness and structural deviation.[13] The V ions are substituted by W ions with different valence states and ion sizes, which inevitably causes a potential disorder in the lattice and further affects the orbital structure.

On the other hand, at 343 K, E_1 and E_2 are 0.607, 0.595, 0.574 eV and 3.576, 3.508, 3.343 eV for S3 ($V_{0.84}W_{0.160}O_{2.002}$), S9 ($V_{0.805}W_{0.195}O_{2.004}$), and S4 ($V_{0.8}W_{0.200}O_{2.006}$), respectively, where the films are at the metal rutile structure. The values obviously decrease with the improvement of the doping level. Figure 10b shows the band scheme of S3 and S4 at the metal state. The split of the d_{II} orbital is still observed at the metal state detected by XAS,[41] which means that dimerization is not accountable for MIT. Meanwhile, MIT in the heavily doping range is only driven by Mott transition. In addition, the π^* orbital is occupied by more doping electrons in the heavily doping range. The value variations of E_2 and $\Delta(E_2 - E_1)$ mean that both the partially filled π^* and filled d_{II} orbitals still shift to a lower energy level toward the O 2p filled π orbital, with increasing W doping concentration. It is opposite to the variation in the light doping range ($x \leq 0.07$).[55] Moreover, the reduction of E_1 at the metal state means that the overlap of the partially filled π^* and filled d_{II} orbitals increased. Meanwhile, the π^* orbital is occupied by more doping electrons when the doping concentration increases.

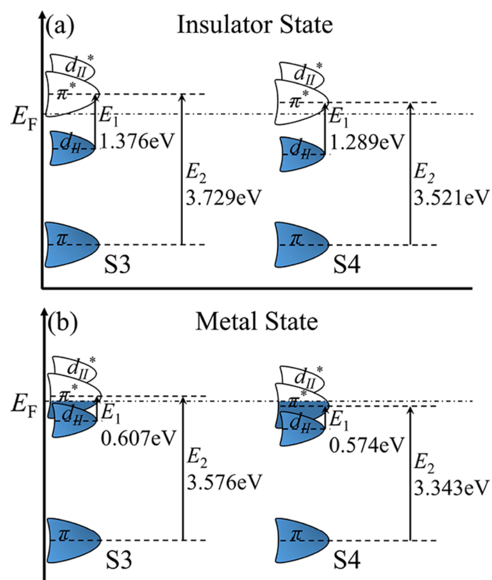

Figure 10. Band scheme of $(S3{\cdot}S4)_{G1}$ at the (a) insulator and (b) metal state with different heavily W-doped concentrations.

The orbital structure plays a significant role in manipulating T_{MIT}. As mentioned above, T_{MIT} increases with increasing x in the heavily doped range, which can be explained by the orbital variation interplay of the insulator monoclinic and metal rutile states. At the metal state, the overlap of the partially filled π^* and filled d_{II} orbitals increases. It can be attributed to the case that the number of doping electrons generated by heavy W doping is increased, with an increasing W doping concentration. Hence, at the metal state, the π^* orbital is occupied by more doping electrons, which further strengthen the electron−electron correlations in the π^* orbital. Moreover, the $V_{1-x}W_xO_2$ film in this range is a representative Mott insulator, where the transition is only driven by strong electron−electron correlation. In a strongly correlated electron system, the increase of d electrons might stabilize the Mott insulator, which needs a higher temperature to transform.[56] In addition, at the insulator and metal states, the π^* and V 3d filled d_{II} orbitals shift toward the O 2p filled π orbital. Meanwhile, at the insulator state, the energy gap between the empty π^* and filled d_{II} orbitals decreases, which further narrows the bandwidth.[56] It is expected to result in the improvement of T_{MIT}.

DOI: 10.1021/acsami.8b09909
ACS Appl. Mater. Interfaces 2018, 10, 30548−30557

The first-principles calculations of the $V_{1-x}W_xO_2$(M) system in the heavily doping range have been performed to provide the theoretical foundation and confirm the above results. As shown in Figure 11a, the calculation of the band structure of the pure insulator monoclinic VO_2 has been carried out along the $Z-\Gamma-Y-A$ direction, with the total DOS, which is in good agreement with the other calculated results.[57−59] In the heavily W doping range, the V atom is replaced by W atom, as shown in Figure 11b. The three typical W/(W + V) atomic ratios, which have been used in the theoretical calculations, are 0.156, 0.188, and 0.219. Figure 11c−e shows the total and partial DOS with different heavy W doping concentrations at the monoclinic structure. It is obvious that the valence and conduction bands slightly move into the lower energy level, which is consistent with the shift of the empty π^* and filled d_{II} orbitals from the experiments. Moreover, the bottom of the conduction band is hybridized by the O 2p, V 3d, and W 5d states. The Fermi level (E_F) is shifted into the conduction band. It indicates that $V_{1-x}W_xO_2$(M) acts as the n-type characteristic,[57] which is different from the pure VO_2(M). It is induced by heavy W doping and the extra d electrons generated by the W atoms. In addition, the theoretically calculated band gap between the valence and conduction bands is decreased from 0.50 to 0.42 eV, with an increasing atomic ratio from 0.156 to 0.219. It is also in agreement with the experimental results, in which the energy gap between the empty π^* and the filled d_{II} orbitals is decreased with increasing heavy W doping concentration.

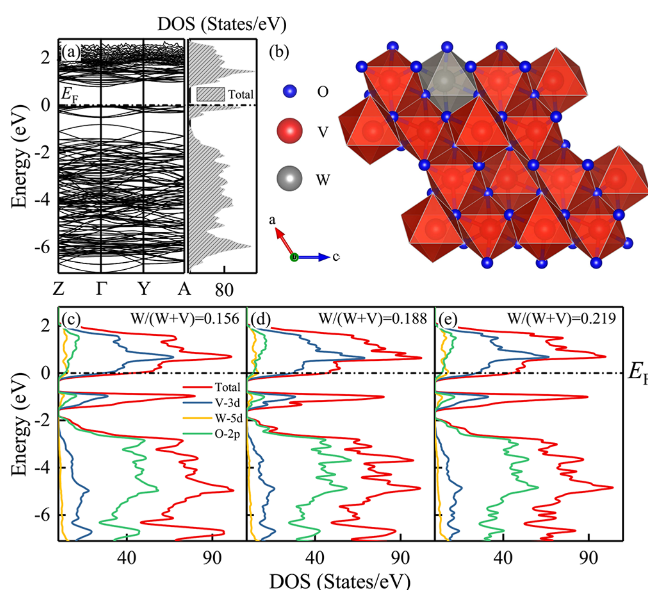

Figure 11. (a) Band structure and total DOS for pure monoclinic VO_2. (b) Schematic of the crystal structure of heavily W-doped VO_2 at the insulator monoclinic structure. (c−e) DOS with different heavily W-doped concentrations at the monoclinic structure.

At the insulator state, the interband electronic transitions E_1 and E_2 are almost unaffected by the oxygen nonstoichiometry.[19] Considering the values of E_1 and E_2 of S2−S4, S7, and S9 at the metal state (at 343 K) from Table 2, we assume that the interband transitions vary linearly with the W doping concentration in the heavily doped range. However, the variation rates of E_2 and $\Delta(E_2 - E_1)$ between S2 and S4 are less than the values between S3 and S4. It indicates that the oxygen vacancies act as the donor dopants to generate extra electrons located at the π^* orbital, which form the localized state and reduce the energy barrier. Meanwhile, the π^* and d_{II} orbitals are slightly closer to the π orbital, which depresses T_{MIT}, in accordance with the calculation results by Chen.[57] In another comparison of the variation rates of S3, S4, and S7, the extra oxygen acts as the acceptor dopant to generate the positively charged vacancy, which recombines with the electron in the π^* orbital and shifts the π^* orbital away from the π orbital. Moreover, it shifts the d_{II} orbital away from the π^* orbital and reduces their overlap, along with increasing T_{MIT}. From the above results, the mechanism of oxygen nonstoichiometry on the phase transition of VO_2 is different from the heavy W doping, which is an important and effective method to control the MIT pattern.

Table 2. Interband Electronic Transitions of the S2−S4, S7, and S9 Films

	insulator state (70 K)		metal state (343 K)	
samp.	E_1 (eV)	E_2 (eV)	E_1 (eV)	E_2 (eV)
S2 $V_{0.811}W_{0.187}O_{1.990}$	1.323	3.602	0.593	3.406
S3 $V_{0.84}W_{0.160}O_{2.002}$	1.376	3.729	0.607	3.576
S4 $V_{0.8}W_{0.200}O_{2.006}$	1.289	3.521	0.574	3.343
S7 $V_{0.822}W_{0.178}O_{2.090}$	1.305	3.634	0.625	3.488
S9 $V_{0.805}W_{0.195}O_{2.004}$	1.286	3.715	0.595	3.508

4. CONCLUSIONS

In summary, the heavily W-doped VO_2 films have been prepared by PLD through controlling three different growth parameters. The influence of heavy W doping ($x \geq 0.10$) on the MIT temperature (T_{MIT}), the complex dielectric function, along with the interband electronic transitions E_1, E_2, and $\Delta(E_2 - E_1)$ has been investigated from the temperature-dependent transmittance spectra, resistivity, and Raman spectra. The feasible mechanism of the orbital structure variation during MIT has been discussed in detail. With increasing W doping concentration, the π^* orbital, along with the lower V 3d filled d_{II} orbital, slightly shifts to the O 2p filled π orbital at the insulator and metal states, which is opposite to the light W doping ($x \leq 0.07$). Meanwhile, the energy gap between the empty π^* and filled d_{II} orbitals decreases at the insulator state. It further narrows the bandwidth and increases T_{MIT}. The first-principles calculations also confirm that the valence and conduction bands slightly move into the lower energy level. The reduction of the energy gap between the valence and conduction bands at the insulator monoclinic structure is verified when the W doping concentration increases. Moreover, the overlap of the π^* and d_{II} orbitals increases at the metal state, and more doping electrons occupy the π^* orbital generated by increasing W dopant. It keeps the Mott insulator more stable and impedes MIT. Finally, the mechanism of oxygen nonstoichiometry on the phase transition of VO_2 has also been investigated, which is different from the heavy W doping. These results reveal that the orbital structure variation plays a critical role in the metal−insulator transition process in the VO_2 system.

DOI: 10.1021/acsami.8b09909
ACS Appl. Mater. Interfaces 2018, 10, 30548−30557

AUTHOR INFORMATION

Corresponding Authors

*E-mail: kjiang@ee.ecnu.edu.cn (K.J.).

*E-mail: zghu@ee.ecnu.edu.cn. Phone: +86-21-54345150. Fax: +86-21-54345119 (Z.H.).

ORCID

Zhigao Hu: 0000-0003-0575-2191

Author Contributions

The manuscript was written through contributions of all authors. All authors have given approval to the final version of the manuscript.

Notes

The authors declare no competing financial interest.

ACKNOWLEDGMENTS

This work was financially supported by National Key Research and Development Program of China (grant no. 2017YFA0303403), Natural Science Foundation of China (grant nos. 61674057 and 61227902), Projects of Science and Technology Commission of Shanghai Municipality (grant nos. 18JC1412400, 18YF1407200, and 18YF1407000), and the Program for Professor of Special Appointment (Eastern Scholar) at Shanghai Institutions of Higher Learning and the Fundamental Research Funds for the Central Universities.

REFERENCES

(1) Chen, F. H.; Fan, L. L.; Chen, S.; Liao, G. M.; Chen, Y. L.; Wu, P.; Song, L.; Zou, C. W.; Wu, Z. Y. Control of the Metal-Insulator Transition in VO2 Epitaxial Film by Modifying Carrier Density. *ACS Appl. Mater. Interfaces* **2015**, *7*, 6875−6881.

(2) Wu, C.; Feng, F.; Xie, Y. Design of Vanadium Oxide Structures with Controllable Electrical Properties for Energy Applications. *Chem. Soc. Rev.* **2013**, *42*, 5157−5183.

(3) Malarde, D.; Powell, M. J.; Quesada-Cabrera, R.; Wilson, R. L.; Carmalt, C. J.; Sankar, G.; Parkin, I. P.; Palgrave, R. G. Optimized Atmospheric-Pressure Chemical Vapor Deposition Thermochromic VO2 Thin Films for Intelligent Window Applications. *ACS Omega* **2017**, *2*, 1040−1046.

(4) Rathi, S.; Lee, I.-y.; Park, J.-H.; Kim, B.-J.; Kim, H.-T.; Kim, G.-H. Postfabrication Annealing Effects on Insulator-Metal Transitions in VO2 Thin-Film Devices. *ACS Appl. Mater. Interfaces* **2014**, *6*, 19718−19725.

(5) Morin, F. J. Oxides Which Show a Metal-to-Insulator Transition at the Neel Temperature. *Phys. Rev. Lett.* **1959**, *3*, 34−36.

(6) Baum, P.; Yang, D.-S.; Zewail, A. H. 4D Visualization of Transitional Structures in Phase Transformations by Electron Diffraction. *Science* **2007**, *318*, 788−792.

(7) Jeong, J.; Aetukuri, N.; Graf, T.; Schladt, T. D.; Samant, M. G.; Parkin, S. S. P. Suppression of Metal-Insulator Transition in VO2 by Electric Field-Induced Oxygen Vacancy Formation. *Science* **2013**, *339*, 1402−1405.

(8) Biermann, S.; Poteryaev, A.; Lichtenstein, A. I.; Georges, A. Dynamical Singlets and Correlation-Assisted Peierls Transition in VO2. *Phys. Rev. Lett.* **2005**, *94*, 026404.

(9) Zhang, P.; Li, M.; Deng, Q.; Zhang, J.; Wu, J.; Hu, Z.; Chu, J. Spectral Assignments in the Infrared Absorption Region and Anomalous Thermal Hysteresis in the Interband Electronic Transition of Vanadium Dioxide Films. *Phys. Chem. Chem. Phys.* **2016**, *18*, 6239−6246.

(10) Morrison, V. R.; Chatelain, R. P.; Tiwari, K. L.; Hendaoui, A.; Bruhács, A.; Chaker, M.; Siwick, B. J. A photoinduced metal-like phase of monoclinic VO2revealed by ultrafast electron diffraction. *Science* **2014**, *346*, 445−448.

(11) Wei, J.; Wang, Z.; Chen, W.; Cobden, D. H. New Aspects of the Metal-Insulator Transition in Single-Domain Vanadium Dioxide Nanobeams. *Nat. Nanotechnol.* **2009**, *4*, 420−424.

(12) Pardo, V.; Pickett, W. E. Half-Metallic Semi-Dirac-Point Generated by Quantum Confinement in TiO2/VO2 Nanostructures. *Phys. Rev. Lett.* **2009**, *102*, 166803.

(13) Zhang, P.; Huang, T.; You, Q.; Zhang, J.; Li, W.; Wu, J.; Hu, Z.; Chu, J. Effects of Crystal Orientation on Electronic Band Structure and Anomalous Shift of Higher Critical Point in VO2 Thin Films during the Phase Transition Process. *J. Phys. D: Appl. Phys.* **2015**, *48*, 485302.

(14) Kalinin, S. V.; Spaldin, N. A. Functional Ion Defects in Transition Metal Oxides. *Science* **2013**, *341*, 858−859.

(15) Sun, X.; Guo, Y.; Wu, C.; Xie, Y. The Hydric Effect in Inorganic Nanomaterials for Nanoelectronics and Energy Applications. *Adv. Mater.* **2015**, *27*, 3850−3867.

(16) Filinchuk, Y.; Tumanov, N. A.; Ban, V.; Ji, H.; Wei, J.; Swift, M. W.; Nevidomskyy, A. H.; Natelson, D. In Situ Diffraction Study of Catalytic Hydrogenation of VO2: Stable Phases and Origins of Metallicity. *J. Am. Chem. Soc.* **2014**, *136*, 8100−8109.

(17) Zhang, Z.; Guo, H.; Ding, W.; Zhang, B.; Lu, Y.; Ke, X.; Liu, W.; Chen, F.; Sui, M. Nanoscale Engineering in VO2 Nanowires via Direct Electron Writing Process. *Nano Lett.* **2017**, *17*, 851−855.

(18) Basu, R.; Sardar, M.; Bera, S.; Magudapathy, P.; Dhara, S. The Role of 1-D Finite Size Heisenberg Chains in Increasing the Metal to Insulator Transition Temperature in Hole Rich VO2. *Nanoscale* **2017**, *9*, 6537−6544.

(19) Zhang, P.; Jiang, K.; Deng, Q.; You, Q.; Zhang, J.; Wu, J.; Hu, Z.; Chu, J. Manipulations from Oxygen Partial Pressure on the Higher Energy Electronic Transition and Dielectric Function of VO2 Films during a Metal-Insulator Transition Process. *J. Mater. Chem. C* **2015**, *3*, 5033−5040.

(20) Zhang, Z.; Zuo, F.; Wan, C. H.; Dutta, A.; Kim, J.; Rensberg, J.; Nawrodt, R.; Park, H. H.; Larrabee, T. J.; Guan, X. F.; Zhou, Y.; Prokes, S. M.; Ronning, C.; Shalaev, V. M.; Boltasseva, A.; Kats, M. A.; Ramanathan, S. Evolution of Metallicity in Vanadium Dioxide by Creation of Oxygen Vacancies. *Phys. Rev. Appl.* **2017**, *7*, 034008.

(21) Kim, M.-W.; Ha, S.-S.; Seo, O.; Noh, D. Y.; Kim, B.-J. Real-Time Structural and Electrical Characterization of Metal-Insulator Transition in Strain-Modulated Single-Phase VO2 Wires with Controlled Diameters. *Nano Lett.* **2016**, *16*, 4074−4081.

(22) Zou, J.; Shi, H.; Su, X.; Feng, Q.; Liang, S. A simple method to prepare V 1-x W x O 2 (x = 0, 0.01, 0.02, 0.03, 0.04, and 0.05) controllable phase transition temperature powder. *J. Alloys Compd.* **2017**, *708*, 706−712.

(23) Karaoglan-Bebek, G.; Hoque, M. N. F.; Holtz, M.; Fan, Z.; Bernussi, A. A. Continuous Tuning of W-Doped VO2 Optical Properties for Terahertz Analog Applications. *Appl. Phys. Lett.* **2014**, *105*, 201902.

(24) Hörlin, T.; Niklewski, T.; Nygren, M. Electrical and magnetic properties of ,. *Mater. Res. Bull.* **1972**, *7*, 1515−1524.

(25) Paik, T.; Hong, S.-H.; Gaulding, E. A.; Caglayan, H.; Gordon, T. R.; Engheta, N.; Kagan, C. R.; Murray, C. B. Solution-Processed Phase-Change VO2 Metamaterials from Colloidal Vanadium Oxide (VOx) Nanocrystals. *ACS Nano* **2014**, *8*, 797−806.

(26) Zhu, J.; Zhou, Y.; Wang, B.; Zheng, J.; Ji, S.; Yao, H.; Luo, H.; Jin, P. Vanadium Dioxide Nanoparticle-based Thermochromic Smart Coating: High Luminous Transmittance, Excellent Solar Regulation Efficiency, and Near Room Temperature Phase Transition. *ACS Appl. Mater. Interfaces* **2015**, *7*, 27796−27803.

(27) Liu, H.; Wan, D.; Ishaq, A.; Chen, L.; Guo, B.; Shi, S.; Luo, H.; Gao, Y. Sputtering Deposition of Sandwich-Structured V2O5/Metal (V, W)/V2O5 Multilayers for the Preparation of High-Performance Thermally Sensitive VO2 Thin Films with Selectivity of VO2(B) and VO2(M) Polymorph. *ACS Appl. Mater. Interfaces* **2016**, *8*, 7884−7890.

(28) Villeneuve, G.; Bordet, A.; Casalot, A.; Pouget, J. P.; Launois, H.; Lederer, P. Contribution to the study of the metal-insulator

DOI: 10.1021/acsami.8b09909
ACS Appl. Mater. Interfaces 2018, 10, 30548−30557

transition in the V1−xNbxO2 system: I - crystallographic and transport properties. *J. Phys. Chem. Solids* **1972**, *33*, 1953−1959.
(29) Hörlin, T.; Niklewski, T.; Nygren, M. Magnetic, electrical and thermal studies on the. *Mater. Res. Bull.* **1973**, *8*, 179−189.
(30) Holman, K. L.; McQueen, T. M.; Williams, A. J.; Klimczuk, T.; Stephens, P. W.; Zandbergen, H. W.; Xu, Q.; Ronning, F.; Cava, R. J. Insulator to Correlated Metal Transition in V1−xMo_xO2. *Phys. Rev. B: Condens. Matter Mater. Phys.* **2009**, *79*, 245114.
(31) Shen, N.; Chen, S.; Chen, Z.; Liu, X.; Cao, C.; Dong, B.; Luo, H.; Liu, J.; Gao, Y. The Synthesis and Performance of Zr-doped and W-Zr-codoped VO2 Nanoparticles and Derived Flexible Foils. *J. Mater. Chem. A* **2014**, *2*, 15087−15093.
(32) Wang, N.; Liu, S.; Zeng, X. T.; Magdassi, S.; Long, Y. Mg/W-Codoped Vanadium Dioxide Thin Films with Enhanced Visible Transmittance and Low Phase Transition Temperature. *J. Mater. Chem. C* **2015**, *3*, 6771−6777.
(33) Wan, D.; Xiong, P.; Chen, L.; Shi, S.; Ishaq, A.; Luo, H.; Gao, Y. High-performance thermal sensitive W-doped VO 2 (B) thin film and its identification by first-principles calculations. *Appl. Surf. Sci.* **2017**, *397*, 30−39.
(34) Chen, R.; Miao, L.; Cheng, H.; Nishibori, E.; Liu, C.; Asaka, T.; Iwamoto, Y.; Takata, M.; Tanemura, S. One-step hydrothermal synthesis of V1−xWxO2(M/R) nanorods with superior doping efficiency and thermochromic properties. *J. Mater. Chem. A* **2015**, *3*, 3726−3738.
(35) Shibuya, K.; Kawasaki, M.; Tokura, Y. Metal-insulator transition in epitaxial V1−xWxO2($0 \leq x \leq 0.33$) thin films. *Appl. Phys. Lett.* **2010**, *96*, 022102.
(36) Asayesh-Ardakani, H.; Nie, A.; Marley, P. M.; Zhu, Y.; Phillips, P. J.; Singh, S.; Mashayek, F.; Sambandamurthy, G.; Low, K.-b.; Klie, R. F.; Banerjee, S.; Odegard, G. M.; Shahbazian-Yassar, R. Atomic Origins of Monoclinic-Tetragonal (Rutile) Phase Transition in Doped VO2 Nanowires. *Nano Lett.* **2015**, *15*, 7179−7188.
(37) Okuyama, D.; Shibuya, K.; Kumai, R.; Suzuki, T.; Yamasaki, Y.; Nakao, H.; Murakami, Y.; Kawasaki, M.; Taguchi, Y.; Tokura, Y.; Arima, T. X-ray Study of Metal-Insulator Transitions Induced by W Doping and Photoirradiation in VO2 Films. *Phys. Rev. B: Condens. Matter Mater. Phys.* **2015**, *91*, 064101.
(38) Takami, H.; Kanki, T.; Ueda, S.; Kobayashi, K.; Tanaka, H. Electronic Structure of W-Doped VO2Thin Films with Giant Metal-Insulator Transition Investigated by Hard X-ray Core-Level Photoemission Spectroscopy. *Appl. Phys. Express* **2010**, *3*, 063201.
(39) Takami, H.; Kanki, T.; Ueda, S.; Kobayashi, K.; Tanaka, H. Filling-Controlled Mott Transition in W-Doped VO2. *Phys. Rev. B: Condens. Matter Mater. Phys.* **2012**, *85*, 205111.
(40) Tan, X.; Yao, T.; Long, R.; Sun, Z.; Feng, Y.; Cheng, H.; Yuan, X.; Zhang, W.; Liu, Q.; Wu, C.; Xie, Y.; Wei, S. Unraveling Metal-Insulator Transition Mechanism of VO2 Triggered by Tungsten Doping. *Sci. Rep.* **2012**, *2*, 466.
(41) Sakai, E.; Yoshimatsu, K.; Shibuya, K.; Kumigashira, H.; Ikenaga, E.; Kawasaki, M.; Tokura, Y.; Oshima, M. Competition between Instabilities of Peierls Transition and Mott Transition in W-Doped VO2 Thin Films. *Phys. Rev. B: Condens. Matter Mater. Phys.* **2011**, *84*, 195132.
(42) Pesquera, D.; Herranz, G.; Barla, A.; Pellegrin, E.; Bondino, F.; Magnano, E.; Sánchez, F.; Fontcuberta, J. Surface Symmetry-Breaking and Strain Effects on Orbital Occupancy in Transition Metal Perovskite Epitaxial Films. *Nat. Commun.* **2012**, *3*, 1189.
(43) Wei, J.; Ji, H.; Guo, W.; Nevidomskyy, A. H.; Natelson, D. Hydrogen Stabilization of Metallic Vanadium Dioxide in Single-Crystal Nanobeams. *Nat. Nanotechnol.* **2012**, *7*, 357−362.
(44) Sun, C.; Yan, L.; Yue, B.; Liu, H.; Gao, Y. The Modulation of Metal-Insulator Transition Temperature of Vanadium Dioxide: a Density Functional Theory Study. *J. Mater. Chem. C* **2014**, *2*, 9283−9293.
(45) Zhang, S.; Kim, I. S.; Lauhon, L. J. Stoichiometry Engineering of Monoclinic to Rutile Phase Transition in Suspended Single Crystalline Vanadium Dioxide Nanobeams. *Nano Lett.* **2011**, *11*, 1443−1447.
(46) Marini, C. Optical Properties of V1−xCr_xO2 Compounds under High Pressure. *Phys. Rev. B: Condens. Matter Mater. Phys.* **2008**, *77*, 235111.
(47) Schilbe, P. Raman Scattering in VO2. *Physica B* **2002**, *316-317*, 600−602.
(48) Baik, J. M.; Kim, M. H.; Larson, C.; Wodtke, A. M.; Moskovits, M. Nanostructure-Dependent Metal−Insulator Transitions in Vanadium-Oxide Nanowires. *J. Phys. Chem. C* **2008**, *112*, 13328−13331.
(49) Jones, A. C.; Berweger, S.; Wei, J.; Cobden, D.; Raschke, M. B. Nano-optical Investigations of the Metal−Insulator Phase Behavior of Individual VO2Microcrystals. *Nano Lett.* **2010**, *10*, 1574−1581.
(50) Zhang, S.; Chou, J. Y.; Lauhon, L. J. Direct Correlation of Structural Domain Formation with the Metal Insulator Transition in a VO2 Nanobeam. *Nano Lett.* **2009**, *9*, 4527−4532.
(51) Silversmit, G.; Depla, D.; Poelman, H.; Marin, G. B.; De Gryse, R. Determination of the V2p XPS Binding Energies for Different Vanadium Oxidation States (V5+ to V0+). *J. Electron Spectrosc. Relat. Phenom.* **2004**, *135*, 167−175.
(52) Manning, T. D.; Parkin, I. P. Atmospheric Pressure Chemical Vapour Deposition of Tungsten Doped Vanadium(IV) Oxide from VOCl3, Water and WCl6. *J. Mater. Chem.* **2004**, *14*, 2554−2559.
(53) Whittaker, L.; Wu, T.-L.; Stabile, A.; Sambandamurthy, G.; Banerjee, S. Single-Nanowire Raman Microprobe Studies of Doping-, Temperature-, and Voltage-Induced Metal-Insulator Transitions of WxV1-xO2 Nanowires. *ACS Nano* **2011**, *5*, 8861−8867.
(54) Goodenough, J. B. The Two Components of the Crystallographic Transition in VO2. *J. Solid State Chem.* **1971**, *3*, 490−500.
(55) He, X.; Zeng, Y.; Xu, X.; Gu, C.; Chen, F.; Wu, B.; Wang, C.; Xing, H.; Chen, X.; Chu, J. Orbital Change Manipulation Metal-Insulator Transition Temperature in W-Doped VO2. *Phys. Chem. Chem. Phys.* **2015**, *17*, 11638−11646.
(56) Imada, M.; Fujimori, A.; Tokura, Y. Metal-insulator Transitions. *Rev. Mod. Phys.* **1998**, *70*, 1039−1263.
(57) Chen, L.; Wang, X.; Wan, D.; Cui, Y.; Liu, B.; Shi, S.; Luo, H.; Gao, Y. Tuning the Phase Transition Temperature, Electrical and Optical Properties of VO2 by Oxygen Nonstoichiometry: Insights from First-Principles Calculations. *RSC Adv.* **2016**, *6*, 73070−73082.
(58) Chen, L.; Cui, Y.; Shi, S.; Liu, B.; Luo, H.; Gao, Y. First-Principles Study of the Effect of Oxygen Vacancy and Strain on the Phase Transition Temperature of VO2. *RSC Adv.* **2016**, *6*, 86872−86879.
(59) Eyert, V. VO2: A Novel View from Band Theory. *Phys. Rev. Lett.* **2011**, *107*, 016401.

DOI: 10.1021/acsami.8b09909
ACS Appl. Mater. Interfaces 2018, 10, 30548−30557